



**HAL**  
open science

## Block Junction-Functionalized All-Conjugated Donor–Acceptor Block Copolymers

Fritz Nübling, Thomas Hopper, Brooke Kuei, Hartmut Komber, Viktoriia Untilova, Simon Schmidt, Martin Brinkmann, Enrique Gomez, Artem Bakulin, Michael Sommer

► **To cite this version:**

Fritz Nübling, Thomas Hopper, Brooke Kuei, Hartmut Komber, Viktoriia Untilova, et al.. Block Junction-Functionalized All-Conjugated Donor–Acceptor Block Copolymers. ACS Applied Materials & Interfaces, 2019, 11 (1), pp.1143-1155. 10.1021/acsami.8b18608 . hal-02045729

**HAL Id: hal-02045729**

**<https://hal.science/hal-02045729>**

Submitted on 9 Dec 2021

**HAL** is a multi-disciplinary open access archive for the deposit and dissemination of scientific research documents, whether they are published or not. The documents may come from teaching and research institutions in France or abroad, or from public or private research centers.

L'archive ouverte pluridisciplinaire **HAL**, est destinée au dépôt et à la diffusion de documents scientifiques de niveau recherche, publiés ou non, émanant des établissements d'enseignement et de recherche français ou étrangers, des laboratoires publics ou privés.

# Block junction-functionalized all-conjugated donor-acceptor block copolymers

*Fritz Nübling<sup>1,‡</sup>, Thomas R. Hopper<sup>1</sup>, Brooke Kuei<sup>#</sup>, Hartmut Komber<sup>§</sup>, Viktoriia Untilova<sup>‡</sup>,  
Simon B. Schmidt<sup>†</sup>, Martin Brinkmann<sup>‡</sup>, Enrique D. Gomez<sup>#,±,||</sup>, Artem A. Bakulin<sup>1</sup>, Michael  
Sommer<sup>†\*</sup>*

<sup>1</sup>Institut für Makromolekulare Chemie, Albert-Ludwigs-Universität Freiburg, Stefan-Meier-  
Straße 31, 79104 Freiburg, Germany

<sup>‡</sup>Freiburger Materialforschungszentrum, Albert-Ludwigs-Universität Freiburg, Stefan-Meier-  
Straße 21, 79104 Freiburg, Germany

<sup>1</sup>Department of Chemistry, Imperial College London, SW7 2AZ, United Kingdom

<sup>#</sup>Department of Material Science and Engineering, The Pennsylvania State University,  
University Park, PA 16802, USA

<sup>±</sup>Department of Chemical Engineering, The Pennsylvania State University, University Park, PA  
16802, USA

<sup>||</sup>Materials Research Institute, The Pennsylvania State University, University Park, PA 16802,  
USA

<sup>§</sup>Leibniz-Institut für Polymerforschung Dresden e.V., Hohe Straße 6, 01069 Dresden, Germany

✚Institut Charles Sadron, CNRS-Universität de Strasbourg, 23 Rue de Loess, 67034 Strasbourg,  
France

┘Technische Universität Chemnitz, Institut für Chemie, Straße der Nationen 62, 09111  
Chemnitz, Germany

Email: [michael.sommer@chemie.tu-chemnitz.de](mailto:michael.sommer@chemie.tu-chemnitz.de)

KEYWORDS: Interfacial electron cascade, P3HT, PNDIT2, donor acceptor block copolymers, all-conjugated block copolymer, transient absorption spectroscopy.

## ABSTRACT

Junction-functionalized donor-acceptor (D-A) block copolymers (BCPs) enable spatial and electronic control over interfacial charge dynamics in excitonic devices such as solar cells. Here we present the design, synthesis, morphology and electronic characterization of block junction-functionalized, all-conjugated, all-crystalline D-A BCPs. Poly(3-hexylthiophene) (P3HT), a single thienylated diketopyrrolopyrrole ( $\text{Th}_x\text{DPPTH}_x$ ,  $x=1$  or  $2$ ) unit and poly{[N,N'-bis(2-octyldodecyl)-naphthalene-1,4,5,8-bis(dicarboximide)-2,6-diyl]-alt-5,5'-(2,2'-bithiophene)} (PNDIT2) is used as donor, interfacial unit and acceptor, respectively. Almost all C-C coupling steps are accomplished by virtue of C-H activation. Synthesis of the macroreagent H-P3HT- $\text{Th}_x\text{DPPTH}_x$ , with  $x$  determining its C-H reactivity, is key to the synthesis of various BCPs of type H-P3HT- $\text{Th}_x\text{DPPTH}_x$ -*block*-PNDIT2. Remarkable morphological behavior is determined from a combination of calorimetry, transmission electron microscopy (TEM) and thin film scattering. Block copolymer crystallinity of P3HT and PNDIT2 is reduced indicating frustrated crystallization. A long period  $l_p$ , is invisible from TEM, but shows up in resonant soft X-ray

scattering experiments on a length scale of  $l_p \sim 60$  nm. Charge transfer photoluminescence of H-P3HT-Th<sub>x</sub>DPPTTh<sub>x</sub> indicates efficient transfer of the excitation energy to the DPP chain end, but is quenched in BCP films. Transient absorption and pump-push-photocurrent spectroscopies reveal geminate recombination (GR) as the main loss channel in as-prepared BCP films independent of junction functionalization. Melt-annealing increases GR as a result of the low degree of crystallinity and poorly defined interfaces, and additionally changes backbone orientation of PNDIT2 from face-on to edge-on. These morphological effects dominate solar cell performance and cause an insensitivity to the presence of the block junction.

## INTRODUCTION

The development of new polymeric materials has enabled ongoing progress in the field of organic photovoltaics (OPV). Aspects such as light absorption, energy levels and charge carrier mobilities, in combination with properties like mechanical stability and flexibility of devices, have been addressed and have led to high performance for non-fullerene-based devices.<sup>1</sup> Beside these advantages, morphology control and reproducibility, as well as thermodynamic stability under operating temperatures remain major challenges for OPV devices made from binary blends of two semiconducting materials. In contrast to small molecules, polymers tend to phase separate because of their low contribution to the entropy of mixing. Manipulating morphology to achieve control over domain size in phase separated donor:acceptor (D:A) structures on the nm length scale is crucial for effective charge generation and transport.<sup>2-4</sup> State-of-the-art methods for empirical morphology control rely on kinetic trapping of phase separation during solution processing, resulting in thermodynamically frozen structures out of equilibrium.<sup>5,6</sup>

Another approach includes ternary mixtures with aligned energy levels to optimize charge separation by multi-step electron cascades to reduce geminate and bimolecular recombination.<sup>7,8</sup> Suitable cascade systems destabilize charge-transfer (CT) states at the interface and therefore reduce recombination to enhance overall OPV performance.<sup>9,10</sup> However, incorporation of a third component into a binary system obviously increases morphological complexity, hence spatial control of individual components is challenging. In addition, mutual energetic interactions can result in mixed energy states at the interface, which is difficult to predict.<sup>11</sup> With these issues pertaining to blending three components, layered systems have been put forward. For an all-polymer, triple layer structured solar cell containing poly(3-hexylthiophene) (P3HT) as the donor, poly{[N,N'-bis(2-octyldodecyl)-naphthalene-1,4,5,8-bis(dicarboximide)-2,6-diyl]-*alt*-5,5'-(2,2'-bithiophene)} (PNDIT2) as the acceptor, and a thin interlayer of poly[N-9''-heptadecanyl-2,7-carbazole-*alt*-5,5-(4',7'-di-2-thienyl-2',1',3'-benzothiadiazole)] (PCDTBT), energy cascades have been reported leading to suppressed charge recombination and enhanced charge lifetimes.<sup>12</sup>

Block copolymers (BCP) are able to form defined phase separated structures that are tunable by molecular weight, volume fraction and intermolecular interactions.<sup>13,14</sup> Such complex polymeric architectures are ideal for the precise positioning of functions at the BCP interface to modulate electronic processes.<sup>15,16</sup> Conjugated BCPs can somewhat differ in chemical structure and phase behavior due to the mostly rigid nature of the conjugated segments, but also due to challenges in chemical synthesis leading to partially ill-defined systems with broader dispersity.<sup>17-20</sup> Single reports have demonstrated that classical diblock copolymer morphologies can be achieved also with conjugated D-A BCPs, if the synthetic approach is highly optimized.<sup>21</sup>

Despite recent progress in this area, the synthesis of well-defined all-conjugated BCPs remains challenging. Only a few examples of all-conjugated, D-A BCPs made by chain growth polymerization have been disclosed.<sup>22,23</sup> The foremost alternative synthetic approach makes use of narrowly distributed poly(3-hexylthiophene) P3HT with well-defined and controllable end group chemistry as a macroreagent.<sup>24-29</sup> To this end, the judicious choice of building blocks and synthetic chemistry can be used to generate different molecular connectivity at the block junction.<sup>27,30-32</sup> These molecular junctions are in conjugation with their adjacent donor and acceptor segments, and hence are electronically unique. From a design point of view regarding BCP junction, it is therefore difficult to predict the effect of molecular connectivity on interfacial charge dynamics, and accordingly, little is known about suitable functionalization strategies and combination of building blocks that result in electron cascade structures when put into conjugation with each other.

Here we report a design strategy for junction-functionalized, all-conjugated, double crystalline donor-acceptor BCPs. As the donor building block, we have selected P3HT due to the unique possibility for simple and quantitative end group functionalization, PNDIT2 as the acceptor block and a single dithienyl-diketopyrrolopyrrole ( $\text{Th}_x\text{DPPTh}_x$ ) unit covalently placed in between both blocks. The choice of these building blocks is based on their electronic complementary properties, leading to an ideal type-II heterojunction,<sup>33</sup> their synthetic compatibility<sup>34</sup> and the fact that the single components have electronic highest occupied molecular orbital (HOMO) and lowest unoccupied molecular orbital (LUMO) levels that form an electronic cascading structure.<sup>35-39</sup> The design of the synthetic sequence employed is based on the rigorous use of C-H activation chemistry. Thus, all C-C coupling steps except P3HT synthesis were accomplished using C-H activation. Key to successful BCP formation is usage of

P3HT-Th<sub>2</sub>DPPT<sub>2</sub> as a macroreagent, which exhibits significantly larger C-H reactivity compared to P3HT-ThDPPT<sub>2</sub>. A series of materials of different molecular weight P3HT-X-*block*-PNDIT<sub>2</sub>, with X being thiophene, ThDPPT<sub>2</sub> or Th<sub>2</sub>DPPT<sub>2</sub>, is synthesized and characterized with respect to molecular, thermal, structural and electronic properties. Thermal and structural analyses evidence a weak tendency for microphase separation, eventually caused by the markedly different crystalline lattice parameters of P3HT and PNDIT<sub>2</sub>. Transient absorption experiments further reveal geminate recombination (GR) in the BCPs a stronger deactivation pathway compared to the blend, with no measurable effect of the DPP block junction on charge dynamics.

## EXPERIMENTAL SECTION

### Materials and Syntheses

Pd<sub>2</sub>dba<sub>3</sub>, Na<sub>2</sub>CO<sub>3</sub>, Cs<sub>2</sub>CO<sub>3</sub>, K<sub>2</sub>CO<sub>3</sub>, <sup>t</sup>Bu<sub>2</sub>PMe \* HBF<sub>4</sub>, P(Me<sub>2</sub>-*p*-anisyl)<sub>3</sub>, P(cy)<sub>3</sub>, DMPP, P(*o*-anisyl)<sub>3</sub>, mesitylene, NBS, Aliquat® 336, Pd(PPh<sub>3</sub>)<sub>4</sub> and pivalic acid were purchased from Sigma-Aldrich and used without further purification. Bithiophene was purchased from ABCR and eluted over SiO<sub>2</sub> with *iso*-hexanes. Freshly prepared Pd<sub>2</sub>dba<sub>3</sub>,<sup>40</sup> ThDPPT<sub>2</sub>,<sup>41-43</sup> Br-ThDPPT<sub>2</sub>-Br,<sup>44</sup> thiophene-2-boronic acid pinacol ester,<sup>45</sup> H-P3HT-Br<sup>46</sup> and NDIBr<sub>2</sub><sup>47,48</sup> were synthesized according to the relevant literature. Synthesis of all-conjugated P3HT-Th-*block*-PNDIT<sub>2</sub> block copolymers was recently reported.<sup>34</sup>

*2,5-Bis(2-ethylhexyl)-3,6-di([2,2'-bithiophene]-5-yl)-2,5-dihydro[3,4-*c*]pyrrol-1,4-dione*  
Th<sub>2</sub>DPPT<sub>2</sub> (2c): 2,5-Bis(2-ethylhexyl)-3,6-di(bromothiophene-2-yl)-2,5-dihydropyrrolo[3,4-*c*]pyrrol-1,4-dione (Br-ThDPPT<sub>2</sub>-Br) (A) (1.0 g, 1.5 mmol), thiophene-2-boronic acid pinacol ester (1.5 g, 7.4 mmol, 4.9 eq) and Pd(PPh<sub>3</sub>)<sub>4</sub> (211.6 mg, 0.2 mmol, 10.0 mol %) were balanced under nitrogen in a reaction flask and tightly closed. The mixture was dissolved in toluene

(10.0 mL, 0.15 M) containing Aliquat<sup>®</sup> 336 and K<sub>2</sub>CO<sub>3</sub> solution (aq., 2.0 M, 5.0 mL) and heated to 90 °C for 72 hours. After cooling to room temperature H<sub>2</sub>O (15.0 mL) was added and the mixture was extracted with CHCl<sub>3</sub> (3 x 25 mL). The combined organic phases have been dried over MgSO<sub>4</sub>, filtered and CHCl<sub>3</sub> was removed at reduced pressure. The product (949.0 mg, 1.4 mmol, 94%) was obtained as dark blue solid.

<sup>1</sup>H NMR (300 MHz, CDCl<sub>3</sub>): δ = 8.95 (d, 2H; a), 7.30-7.36 (m, 6H; b; c; e), 7.08 (dd, 2H; d), 4.05 (m, 4H; 1), 1.93 (m, 2H; 2), 1.21-1.44 (m, 16H; 3-5; 7), 0.81-0.95 ppm (m, 6H; 6; 8).

MS (ESI): m/z = 688.2285 [M], 689.2347 [M-H]<sup>+</sup>, 711.2178 [M-Na]<sup>+</sup>.

Elemental analysis: Calculated (%) C 66.24, H 6.44, N 4.07, S 18.61. Found (%) C 61.64, H 6.16, N 3.27, S 17.92.

*Standard procedure for H-P3HT-ThDPPT<sub>h</sub> synthesis (3b):* A dry 4 mL screw-cap vial containing a stir bar was charged with H-P3HT-Br (**1**) (42.6 mg, 6.1 μmol), ThDPPT<sub>h</sub> (**2b**) (66.5 mg, 127 μmol, 20.9 eq), Cs<sub>2</sub>CO<sub>3</sub> (8.2 mg, 25.2 μmol, 4.1 eq), PivOH (0.8 mg, 7.8 μmol, 1.3 eq), Pd<sub>2</sub>dba<sub>3</sub> (0.2 mg, 0.2 μmol, 3.6 mol %) and P-(*o*-anisyl)<sub>3</sub> (0.2 mg, 0.5 μmol, 8.0 mol %), evaporated with vacuum and flushed with nitrogen three times in a row. Mesitylene (0.64 mL, 0.2 M), degassed with nitrogen, was added and the reaction mixture was heated up to 100 °C for 72 hours. After cooling to room temperature, the crude product was precipitated in excess methanol and extracted with methanol, acetone and *iso*-hexanes. The product was purified by dissolving in chloroform and filtering over SiO<sub>2</sub>. The solvent was evaporated by reduced pressure and the P3HT-ThDPPT<sub>h</sub> polymers were obtained as a thin film in quantitative yields. The same procedure has been followed by syntheses of H-P3HT-Th<sub>2</sub>DPPT<sub>h</sub> (**3c**) by replacing **2b** with Th<sub>2</sub>DPPT<sub>h</sub> (**2c**) as end group function.

*Standard procedure for H-P3HT-ThDPPT<sub>h</sub>-block-PNDIT<sub>2</sub> block copolymer reactions (4b):* P3HT-ThDPPT<sub>h</sub> (**3b**) (33.5 mg, 4.8  $\mu$ mol, 0.1 eq), NDIBr<sub>2</sub> (47.2 mg, 47.9  $\mu$ mol), bithiophene (7.6 mg, 45.7  $\mu$ mol, 0.95 eq), Na<sub>2</sub>CO<sub>3</sub> (15.5 mg, 146.0  $\mu$ mol, 3.1 eq), pivalic acid (5.6 mg, 54.8  $\mu$ mol, 0.8 eq) and Pd<sub>2</sub>dba<sub>3</sub> (0.6 mg, 0.7  $\mu$ mol, 1.4 mol %) were added into a screw-cap vial containing a stir bar, evaporated with vacuum and flushed with nitrogen three times in a row. In the same time, mesitylene (0.48 mL, 0.1 M) was degassed with nitrogen for at least 20 minutes and added to the reaction mixture by syringe. Afterwards the vial was tightly sealed and the polymerization was started at 90 °C for 72 h. Afterwards, the mixture was cooled down, diluted with chloroform, precipitated into excess methanol and filtered. The precipitated crude product was further purified by Soxhlet extraction with methanol, acetone, ethyl acetate, *iso*-hexanes, dichloromethane and chloroform, respectively. The obtained dichloromethane and chloroform fractions were separately filtered over SiO<sub>2</sub> before evaporation of the solvent. The same procedure has been followed by the syntheses of *H-P3HT-Th<sub>2</sub>DPPT<sub>h</sub>-block-PNDIT<sub>2</sub> (4c)* by replacing **3b** with **3c** as terminating reagent.

### **Instruments**

*NMR Spectroscopy.* NMR spectra of polymer samples were recorded on a Bruker Avance III 500, and DPP monomers on a Bruker Avance 300 spectrometer. CDCl<sub>3</sub> and C<sub>2</sub>D<sub>2</sub>Cl<sub>4</sub> (at 120 °C) were used as solvents. The spectra were referenced to the residual solvent peak (CDCl<sub>3</sub>:  $\delta(^1\text{H}) = 7.26$  ppm, C<sub>2</sub>D<sub>2</sub>Cl<sub>4</sub>:  $\delta(^1\text{H}) = 5.98$  ppm).

*Gel Permeation Chromatography.* GPC measurements of all samples were carried out on four SDV gel 5  $\mu$ m columns with pore sizes ranging from 10<sup>3</sup> to 10<sup>6</sup> Å (Polymer Standards), connected in series with a Knauer K-2301 RI detector and a G1314B UV detector (Agilent

Technologies) calibrated with polystyrene standards.  $\text{CHCl}_3$  was used as eluent at 22 °C with a flow rate of 1.0 mL/min.

*UV-vis Spectroscopy.* UV-vis spectra were recorded at 25 °C on a UV-1800 Series (Shimadzu) in chloroform solutions ( $c = 0.02$  mg/mL), or as thin films on glass substrates, spun cast from chlorobenzene (12 mg/mL).

*Photoluminescence.* PL spectra were recorded at 25 °C with a HPX-2000 xenon lamp, a MonoScan2000 monochromator (Mikropack) and a S2000-FL detector (Ocean Optics) in chloroform solutions ( $c = 0.02$  mg/mL) or as thin films on glass substrates. Samples were excited with an argon-ion laser at 450 nm and recorded in a 90° angle to the light source from 465 nm to 900 nm.

*Cyclic voltammetry.* CV measurements of thin films were done at room temperature with a PalmSens4 potentiostat in dry MeCN with  $\text{NBu}_4\text{PF}_6$  (0.1 M) as electrolyte. Samples were coated onto the glassy carbon working electrode and measured under Argon with a scan rate of 50 mV/s. All curves have been shifted versus ferrocene standard.

*Matrix-assisted laser desorption/ionization – time of flight mass spectrometry.* MALDI-ToF MS spectra were recorded on an Autoflex III mass spectrometer (Bruker). Samples were prepared as 5-10 mg/mL solutions.

*Mass spectrometry.* ESI-MS spectra have been recorded in FTMS + p ESI Full lock ms mode on a LCQ Extractive (Thermo Scientific).

*Differential Scanning Calorimetry.* DSC measurements were carried out on a DSC Seiko 6200 (Seiko/Perkin Elmer) under nitrogen atmosphere. Heating and cooling rates were 10 K/min. The mass of the samples for each measurement was approximately 3-5 mg.

*Device fabrication.* OPV devices were fabricated to give the following device structure: glass/ITO/PEDOT:PSS/polymer/Ca/Al/glass. ITO covered glass slides were first cleaned with acetone and then isopropanol for 10 minutes under ultrasound before treated by oxygen plasma for 20 minutes. PEDOT:PSS was spin-coated to give a  $\sim 35$  nm layer and annealed at 160 °C for 20 minutes. The substrates were introduced into a nitrogen-filled glove box. The photoactive polymer layer was spin-coated from 12 mg/ml chlorobenzene solution to yield 70 nm thin films, which were subjected to different annealing protocols. Afterwards, hole blocker Ca (20 nm) has been evaporated on the active layer prior to the aluminum electrode ( $\sim 100$  nm). For TA measurements, devices have been encapsulated with glass using epoxy resin.

*Device testing.* *JV* characteristics were measured under AM 1.5 illumination ( $100 \text{ mW/cm}^2$ ) using an Abet Technology solar simulator. Currents were recorded using a Keithley 237 source meter. Spectral mismatches of the simulator were calibrated with a silicon reference cell.

*Elemental analysis.* EA measurements have been performed with a vario MICRO cube (Elementar Analysensysteme GmbH) for quantitative determination of C, H, N and S. Samples have been transported with He and O<sub>2</sub> gas for controlled decomposition at 1150 °C and resulting gases have been detected with a thermal conductivity detector.

*Transient Absorption spectroscopy.* For TAS, a 1 kHz Ti:sapphire regenerative amplifier (Spectra-Physics Solstice, Newport Corporation) provided seed pulses (800 nm,  $\sim 100$  fs) for the pump and probe. The pump was generated by an optical parametric amplifier (TOPAS, Light Conversion) coupled to a frequency mixer (NIRUVis, Light Conversion), while the broadband NIR probe ( $\sim 850$ -1350 nm) was generated in an yttrium aluminium garnet crystal inside the commercially available TAS setup (HELIOS, Ultrafast Systems). The pump and probe were focused onto a  $0.5 \text{ mm}^2$  spot on the sample, which was placed in a N<sub>2</sub>-purged cuvette for

measurements. The pump was modulated at 500 Hz, and the delay between the pump and probe was controlled with a mechanical stage in the probe beam path. All analyses were conducted in MATLAB and Origin.

*Pump-push-photocurrent spectroscopy.* Two optical parametric amplifiers (TOPAS-Prime, Coherent) were seeded with 800 nm, ~35 fs pulses from a 4 kHz Ti:sapphire regenerative amplifier (Astrella, Coherent). The 1400 nm signal output from one TOPAS was frequency-doubled in a  $\beta$ -barium borate crystal to generate the 700 nm pump. The 2000 nm idler output from the other TOPAS was used as the push, and modulated by an optical chopper at ~1.2 kHz. The pump and push were directed onto a ~0.5 mm<sup>2</sup> spot on the devices. The push- and pump-induced photocurrent ( $dJ$  and  $J$ , respectively) were measured at their respective modulation frequencies (1.2 kHz and 4 kHz) by a lock-in amplifier (SR830, Stanford Research Systems). The delay between the pump and push pulses was controlled by delaying the pump with a mechanical delay stage.

*High-resolution transmission electron microscopy.* HR-TEM was performed in low dose mode on a FEI CM12 microscope equipped with a mega view III CCD camera (Soft Imaging System). For sample preparation, the films were first coated with a thin film of amorphous carbon using an Auto 306 Edwards evaporator under high vacuum ( $10^{-5}$ - $10^{-6}$  mbar). The films were removed from their Si(100) substrates using polyacrylic acid, floated on distilled water and recovered on TEM copper grids. Thermal treatments of the films on the TEM grids were performed in a linkam LTS420 hot stage (310°C for 10 min.) under nitrogen flow. Specific conditions for HR-TEM and low dose diffraction are given elsewhere.<sup>49</sup>

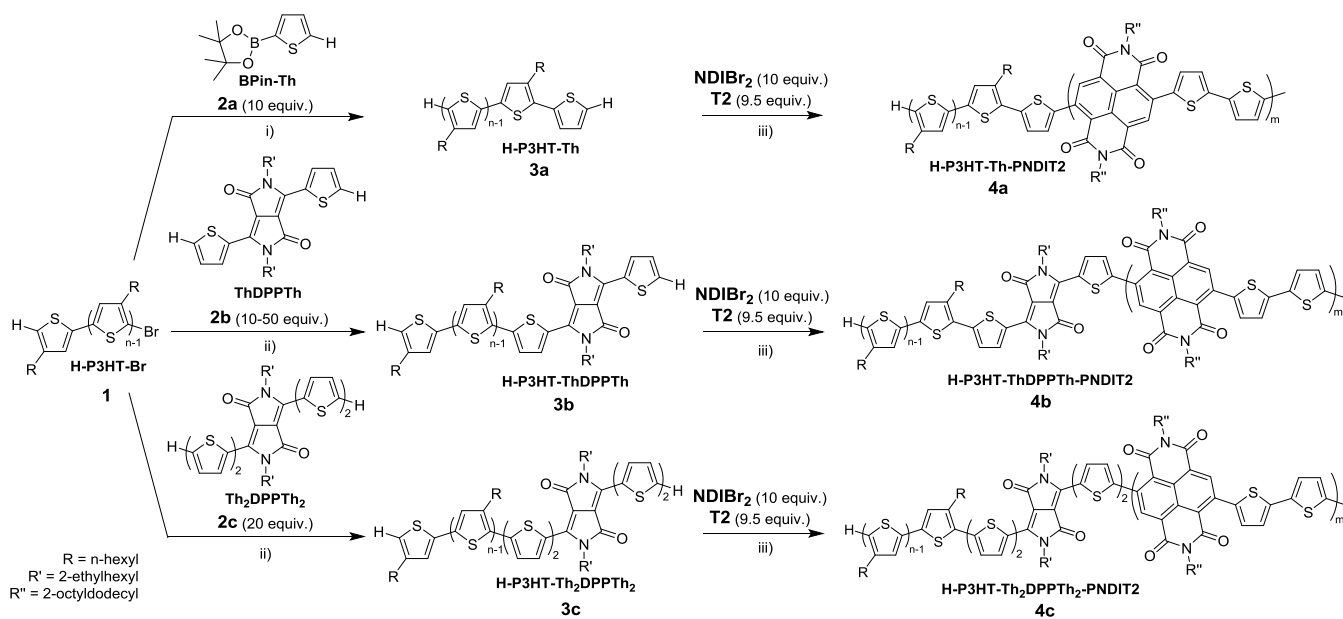
*Resonant Soft X-ray scattering.* 12 mg/mL solutions were dissolved in 1-chlorobenzene overnight at 70 °C. For each sample, 35  $\mu$ L of solution was deposited on a 50 nm Si<sub>3</sub>N<sub>4</sub> window

with a 5 mm x 5 mm silicon frame (Norcada) at 1000 rpm for 60 s then 4000 rpm for 10 s, resulting in polymer films with thickness ca. 60-70 nm. Samples were then annealed in the melt at 310 °C for 30 minutes in a N<sub>2</sub> glovebox and then cooled at 10 K/min. RSoXS experiments were carried out at beamline 11.0.1.2 at the Advanced Light Source at Lawrence Berkeley National Laboratory in transmission geometry under vacuum at various X-ray energies around 284 eV with linear polarization. A sample to detector distance of 50 mm was used to cover a  $q$  range of 0.004 Å<sup>-1</sup> to 0.06 Å<sup>-1</sup> ( $q = 4\pi \sin(\theta/2)/\lambda$ , where  $\lambda$  is the X-ray wavelength and  $\theta$  is the scattering angle). Data were radially integrated and presented as a function of  $q$ . RSoXS data were corrected for dark currents.

## RESULTS AND DISCUSSION

The chemical design strategy towards P3HT-*X-block*-PNDIT2 started with appropriate mono-functionalization of P3HT by X, which can in principle be achieved using functional initiators, in-situ end capping or a combination of the two. Continuing previous work,<sup>34</sup> we used H-P3HT-Br (**1**) made via KCTP,<sup>46</sup> followed by end group functionalization with ThDPPT<sub>h</sub> (**2b**) under direct arylation conditions (Scheme 1). Afterwards, optimized reaction conditions have been successfully transferred towards Th<sub>2</sub>DPPT<sub>h</sub> (**2c**). The two-step synthesis of **2c** and the analysis by <sup>1</sup>H NMR spectroscopy are shown in detail in the supporting information (Scheme SI-1 and Figure SI-1). In all cases, P3HT **1** had a  $M_{n,NMR}$  of ~ 7.0 kg/mol ( $DP_{n,NMR}$  ~42) and a  $M_{n,SEC}$  of around 11 kg/mol with dispersities <1.10. While the synthesis of **3a** via Suzuki coupling has been described elsewhere,<sup>34</sup> optimization of end group functionalization of **1** with **2b** has been done by direct C-H arylation.

**Scheme 1.** End group functionalization of H-P3HT-Br (**1**) with BPin-Th (**2a**) to H-P3HT-Th (**3a**) by Suzuki coupling, ThDPPTTh (**2b**) to H-P3HT-ThDPPTTh (**3b**) and Th<sub>2</sub>DPPTTh<sub>2</sub> (**2c**) to H-P3HT-Th<sub>2</sub>DPPTTh<sub>2</sub> (**3c**) under direct C-H arylation and further use as macroreagent in direct C-H polycondensation of NDIBr<sub>2</sub> and T2 for syntheses of block copolymers H-P3HT-Th-*block*-PNDIT2 (**4a**), H-P3HT-ThDPPTTh-*block*-PNDIT2 (**4b**) and H-P3HT-Th<sub>2</sub>DPPTTh<sub>2</sub>-*block*-PNDIT2 (**4c**).<sup>a</sup>



<sup>a</sup>Reaction conditions: i) Pd(PPh<sub>3</sub>)<sub>4</sub> (5 mol %), Cs<sub>2</sub>CO<sub>3</sub> (3 equiv.), solvent THF, 80 °C, 72 h. ii) Pd<sub>2</sub>dba<sub>3</sub> (4 mol %), P(o-anisyl)<sub>3</sub> (16 mol %), Cs<sub>2</sub>CO<sub>3</sub> (3 equiv.), PivOH (1 equiv.), solvent mesitylene (0.1 M), 100 °C, 72 h. iii) Pd<sub>2</sub>dba<sub>3</sub> (1 mol %), PivOH (1 equiv.), Na<sub>2</sub>CO<sub>3</sub> (3 equiv.), solvent mesitylene (0.1 M).

Significant reaction parameter screening was necessary to get **3b** with almost quantitative end group conversion. Screening of reaction parameters included variations of palladium catalyst precursor, phosphine ligands, excess of **2b** and reaction temperature, enabling complete conversion and end group functionalization as depicted in Scheme 1. Description of reaction condition optimizations towards H-P3HT-ThDPPTTh (**3b**) are summarized in the supporting information (Table SI-1).

Overall, the highest yield (95%) was obtained with fresh prepared Pd<sub>2</sub>dba<sub>3</sub> catalyst, with tris(*o*-methoxyphenyl)phosphine (P(*o*-anisyl)<sub>3</sub>) as ligand, at 100 °C with 20 equivalents of **2b**. Excess of **2b** can be recycled completely during Soxhlet workup without further purification. This protocol was transferred to the reaction with Th<sub>2</sub>DPPTTh<sub>2</sub>(**2c**), giving acceptable 93% end group functionalization of **3c**. Complete analyses of **3b** and **3c** by <sup>1</sup>H NMR spectroscopy, MALDI-ToF MS and SEC are detailed in the supporting information in Figure SI-2-9.

Successful synthesis of H-P3HT-ThDPPTTh and H-P3HT-Th<sub>2</sub>DPPTTh<sub>2</sub> allowed for BCP synthesis with **3b** and **3c** as macroreagent in copolymerization of NDIBr<sub>2</sub> and T2 under direct arylation conditions.<sup>34,50</sup> In Scheme 1, BCP synthesis with thiophene (Th) and diketopyrrolopyrrole (Th<sub>x</sub>DPPTTh<sub>x</sub>, x=1, 2) functionalized P3HTs are depicted together. Despite the structurally similar end groups of P3HT-Th-H, P3HT-ThDPPTTh-H and P3HT-Th<sub>2</sub>DPPTTh<sub>2</sub>-H, BCP synthesis as shown in Scheme 1 resulted in products of different composition and BCP architecture. For all three macroreagent, the reactivity of the proton next to the hexyl side chain is sufficiently low, resulting in a minor incorporation of P3HT with the non-functionalized side of the polymer chain. If so, the resulting BCP architectures will contain a minor fraction of triblock-type PNDIT2-*block*-P3HT-X-*block*-PNDIT2. For simplicity, however, Scheme 1 shows here diblock copolymer structures only. Regarding C-H reactivity at the other side of the functionalized P3HT endcapper, i.e. X, the three different compounds **3a-c** exhibited significantly different reactivity. While usage of P3HT-Th-H (**3a**) enabled complete incorporation of P3HT into BCP **4a**, the significantly lower C-H reactivity of P3HT-ThDPPTTh-H (**3b**) resulted in a mixture of unreacted **3b** and BCP **4b**. In contrast, the C-H bond of the DPP-bithiophene end group of P3HT-Th<sub>2</sub>DPPTTh<sub>2</sub>-H (**3c**) showed increased reactivity, resulting in complete end group conversion similar to **4a**. The lower C-H reactivity of **3b** compared to **3c**

likely stems from the electron-deficient DPP core that renders the thiophene end group in **3b** less electron-rich compared to T2 in **3c**. Reason for the T2 linker between P3HT and the DPP core in **3c** is therefore of synthetic nature and simply guarantees complete end group functionalization. Thus, we are able to synthesize a set of BCPs with different end group functionalized H-P3HT-X macroreagents to obtain fully conjugated BCPs with (**4c**) and without (**4a**) DPP junction functionalization. Different molecular weights  $M_{n,SEC}$  between 19 and 57 kg/mol were obtained using previously established protocols.<sup>34</sup> By applying the same stoichiometric ratio for all BCP syntheses, samples with compositions between 33 and 43 wt % P3HT were obtained, whereby a larger molecular weight is correlated with slightly larger P3HT fractions (Table 1).

**Table 1.** Molecular properties of BCP samples P3HT-X-*block*-PNDIT2, X = Th (**4a**), ThDPPTTh (**4b**) and Th<sub>2</sub>DPPTTh<sub>2</sub> (**4c**).

sample	junction X=	$M_{n,SEC}$ BCP/ kg/mol <sup>a</sup>	$\mathbf{D}^a$	$M_{n,SEC}$ P3HT/ kg/mol <sup>b</sup>	P3HT/ wt % <sup>c</sup>	P3HT/ mol % <sup>c</sup>	conversion end groups H-P3HT / P3HT-X/ % <sup>d</sup>
<b>4a</b> -23K	Th	23 <sup>a</sup>	1.8	11.6	37	78	16/100
<b>4a</b> -49K	Th	49 <sup>b</sup>	1.9	11.6	43	82	22/100
<b>4a</b> -57K	Th	57 <sup>b</sup>	2.0	11.6	42	81	24/100
<b>4b</b> -34K	ThDPPTTh	34 <sup>b</sup>	1.9	10.8	38	78	28/75
<b>4c</b> -19K	Th <sub>2</sub> DPPTTh <sub>2</sub>	19 <sup>a</sup>	1.8	12.3	33	75	17/100
<b>4c</b> -42K	Th <sub>2</sub> DPPTTh <sub>2</sub>	42 <sup>b</sup>	2.0	12.3	42	81	19/100
<b>4c</b> -57K	Th <sub>2</sub> DPPTTh <sub>2</sub>	57 <sup>b</sup>	2.3	13.1	38	79	37/100

<sup>a</sup>From SEC in CHCl<sub>3</sub> after Soxhlet extraction with methanol, acetone, ethyl acetate and *iso*-hexane. <sup>b</sup>From SEC in CHCl<sub>3</sub> after Soxhlet extraction with methanol, acetone, ethyl acetate, *iso*-hexane and dichloromethane. <sup>c</sup>From <sup>1</sup>H NMR integrals of the methylene group at 4.19 ppm (NCH<sub>2</sub> of NDI) and 2.86 ppm ( $\alpha$ -CH<sub>2</sub> of P3HT). <sup>d</sup>From <sup>1</sup>H NMR integrals of the linkage signal at 7.18 ppm and the P3HT-H end group signal at 6.94 ppm. Conversion of P3HT-X from comparison with the signal integrals of pristine H-P3HT-X. Estimated error:  $\pm 5$  %.

A detailed BCP analysis by wavelength-dependent SEC enables characterization of individual blocks. Detection at 450 nm (red curve) is ascribed almost exclusively to P3HT alone (for UV-vis in solution see also Figure 5a), whereas at 600 nm (green curve) any species carrying PNDIT2 segments can be observed.<sup>34</sup> Signals detected at 254 nm consider both species. Thus, in general, the more congruent the three curves are, the more homogeneous the product, i.e. the less

homopolymer impurities are contained. In Figure 1, the size exclusion chromatography (SEC) traces of the products recorded at different wavelengths show formation of block copolymers due to overlap of the 450 nm and 600 nm curves. Overlapping curve parts can be assigned to the P3HT and PNDIT2 homopolymers. The sharp signal at 37.5 mL (450 nm) stems from the P3HT homopolymer. Importantly, while this signal in Figure 1b is due to unreacted P3HT-ThDPPTh, the same signal of lower intensity in Figure 1c is from P3HT-H that results from dehalogenation during reaction with Th<sub>2</sub>DPPTh<sub>2</sub>, and hence is contained already in **3c**. While it is clear that detection at 450 nm (red curve) overestimates the amount of residual P3HT, quantification from wavelength-dependent SEC is difficult due to different extinction coefficients of the individual components. A complete comparison of SEC elugrams of all BCP samples **4a** and **4c** summarized in Table 1 is available in the supporting information (Figure SI-10).

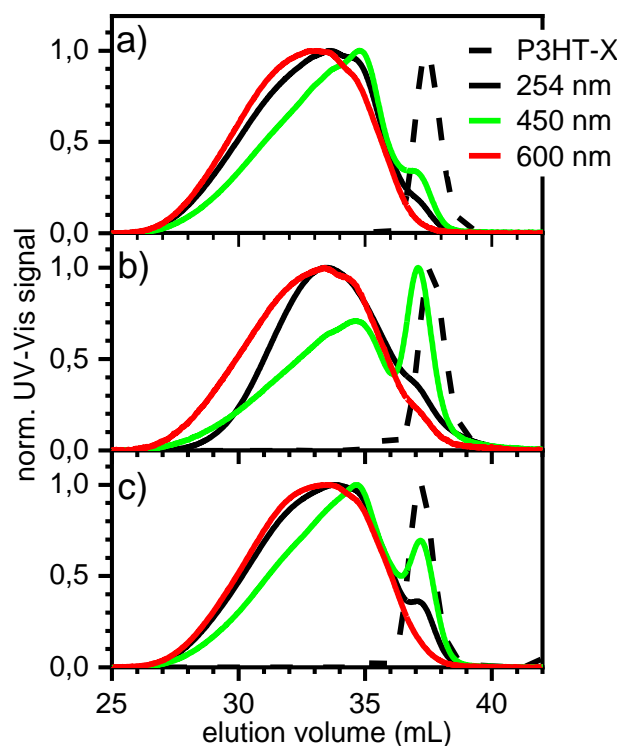


**Figure 1.** Wavelength-dependent SEC spectra of block copolymers a) H-P3HT-Th-*block*-PNDIT2 (**4a**-49K), b) H-P3HT-ThDPPTTh-*block*-PNDIT2 (**4b**-34K) and c) H-P3HT-Th<sub>2</sub>DPPTTh<sub>2</sub>-*block*-PNDIT2 (**4c**-42K).

For a quantitative analysis of **4b** and **4c**, <sup>1</sup>H NMR spectroscopy was employed (Figures 2 and 3). Figure 2 comprises the chemical structures (a) together with <sup>1</sup>H NMR spectra of **4b** (b) and **3b** (c) with assigned protons. Formation of PNDIT2 copolymer in **4b** is obvious from the new backbone signals at 7.45 ppm (T2 unit) and at 9.3 ppm (NDI unit). Characteristic T2 end groups are indicated by purple color.<sup>50</sup> Due to the reaction of the DPPTTh-H end groups (light green) with NDI-Br leading to the block junction -DPPTTh-NDI-, new signals appear (blue) and prove BCP formation. A detailed assignment of these signals based on <sup>1</sup>H-<sup>1</sup>H COSY is given in Figure SI-11.

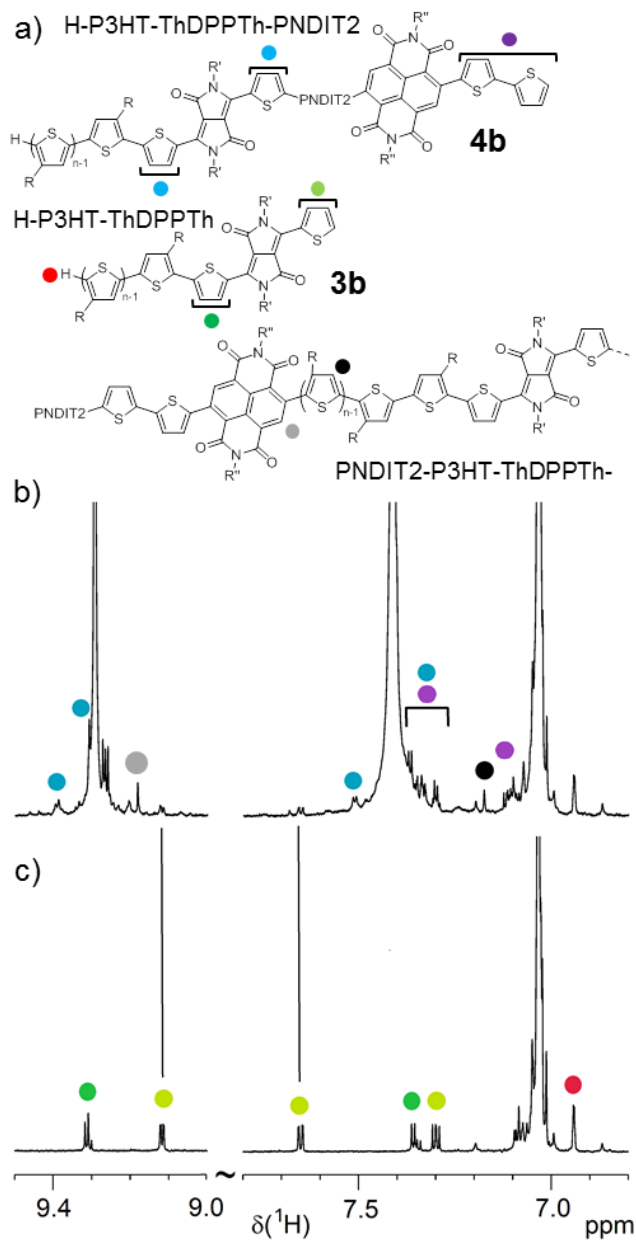


**Figure 2.** a) Chemical structures and  $^1\text{H}$  NMR spectra (aromatic region) of b) -ThDPPTTh- block junction functionalized BCP **4b** and c) P3HT-ThDPPTTh **3b** ( $\text{C2D2Cl4}$ ,  $120\text{ }^\circ\text{C}$ ).

Residual signals of the -DPPTTh-H end groups in the BCP spectrum indicate an incomplete reaction with 70-80% conversion. Signals at 9.18 ppm (grey) and 7.18 ppm (black) point to the mentioned side reaction involving reaction of the H-P3HT group of **3b**. The hexyl group in  $\alpha$

position does not completely prevent direct C-H arylation of this end group, resulting in formation of triblock copolymers. From the integrals of these signals and the residual P3HT-H end group signal a conversion of about 25-30% is estimated (Table 1). We envisioned incomplete conversion of the DPPTh-H EG in **3b** being caused by the electron deficient nature of the adjacent DPP core, and therefore performed the same reaction sequence with P3HT-Th<sub>2</sub>DPPTh<sub>2</sub> (Scheme 1). The comparison of <sup>1</sup>H NMR spectra of product **4c** and precursor **3c** is shown in Figures 3.

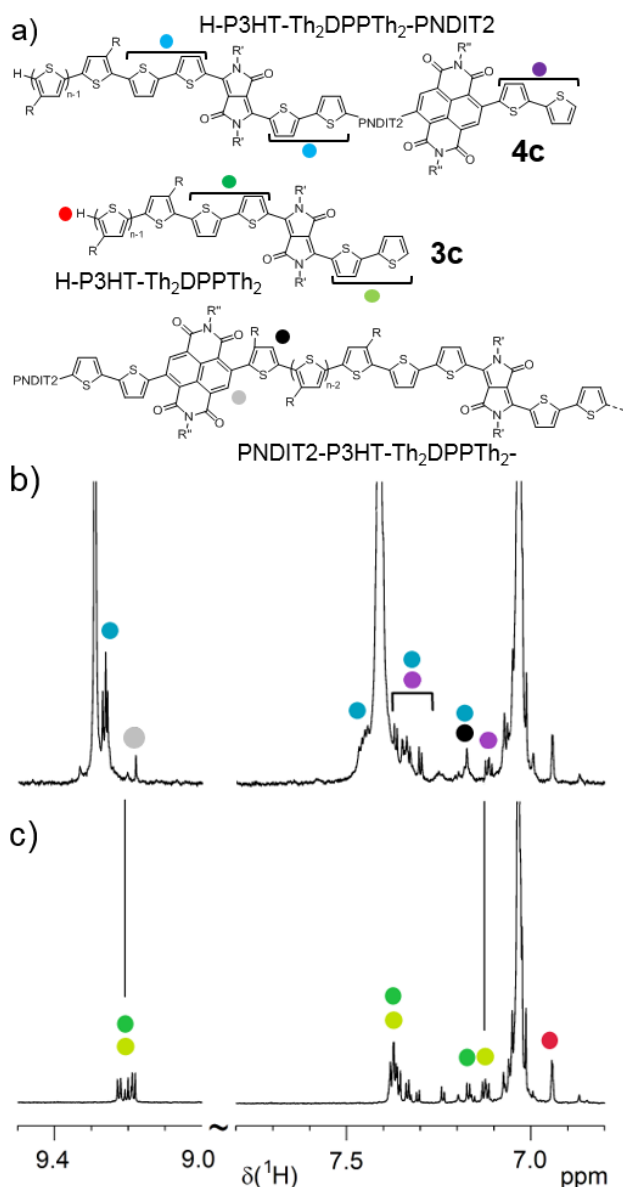


**Figure 3.** a) Chemical structures and  $^1\text{H}$  NMR spectra (aromatic region) of b)  $-\text{Th}_2\text{DPPTTh}_2-$  block junction functionalized BCP **4c** and c) precursor H-P3HT- $\text{Th}_2\text{DPPTTh}_2$  **3c** ( $\text{C}_2\text{D}_2\text{Cl}_4$ ,  $120\text{ }^\circ\text{C}$ ).

To our content, complete conversion of  $-\text{DPPTTh}_2-\text{H}$  end groups of **3c** (green) can be concluded. Unfortunately, most signals of the junction group overlap with both the NDI as well as the T2 signal of the PNDIT2 block. Besides the new PNDIT2 end groups (purple), new signals (black and grey) occur because of the conversion of the H-P3HT end group. For complete conversion of  $-\text{DPPTTh}_2-\text{H}$  end group, only 19% of all H-P3HT end groups are converted, indicating the higher reactivity of  $-\text{DPPTTh}_2-\text{H}$  in comparison to  $\text{DPPTTh}-\text{H}$ , and thus a higher selectivity between  $-\text{DPPTTh}_2-\text{H}$  and H-P3HT compared to  $-\text{DPPTTh}-\text{H}$  and H-P3HT. Extension of dithienyl-DPP with thiophene to give **3c** therefore results in the successful preparation of DPP block junction functionalized BCPs **4c**.

The thermal properties of the BCPs were investigated by differential scanning calorimetry (DSC) to gain information about thermal transitions and microphase separation behavior (Figure 4). All DSC traces of BCPs were investigated as a function of molecular weight, and compared with P3HT and PNDIT2 homopolymers of similar molecular weight and also a P3HT:PNDIT2 blend prepared in solution (Table 1 and 2). Polymers used in blend are almost equal (P3HT) or the same (PNDIT2) regarding molecular weights and dispersities of used homopolymers in DSC measurements. From Figure 4 and Table 2 three main results can immediately be deduced: i) all BCP samples exhibit two, albeit weak, transitions, ii) the melting and crystallization enthalpies  $\Delta H_m$  and  $\Delta H_c$  are significantly smaller compared to the homopolymers and the blend, and iii) the crystallization temperatures  $T_c$  are lower due to undercooling.

Estimated enthalpies indicate partial crystallization of both polymer blocks, thus are not representative for polymer compositions. Increasing the content of triblock BCPs, as observed for **4c-57K**, results in the suppression of melting and crystallization signals because of reduced segmental mobility of the chains.<sup>51</sup> Interestingly, the first and second series of comparable samples, **4a-23K** vs **4c-19K** and **4a-49K** vs **4c-42K**, show a higher crystallinity of BCP samples with DPP junction functionalization at almost equal H-P3HT conversion. Overall, the reduced degrees of crystallinity for both blocks suggest that microphase separation is hampered.<sup>25</sup>

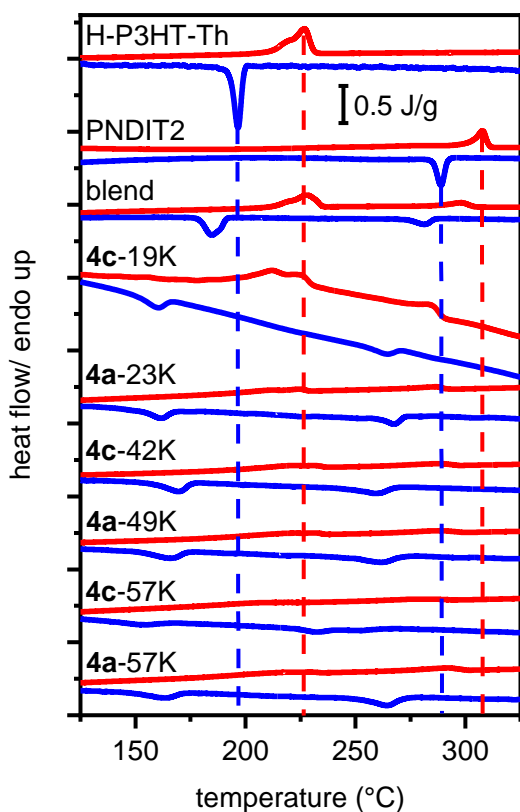


**Figure 4.** DSC curves of homopolymers P3HT and PNDIT2, blend P3HT:PNDIT2 (40:60 wt %), samples **4a** and **4c**. In all cases heating (red upper curve) and cooling (blue lower curve) was measured at 10 K/min. Melting (red) and crystallization (blue) peaks of homopolymers P3HT and PNDIT2, respectively, are marked with dashed lines.

**Table 2.** Melting and crystallization enthalpies of P3HT, PNDIT2, blend P3HT:PNDIT2 (40:60 wt %) and BCP samples **4a** and **4c**. Heating and cooling rates are 10 K/min for all listed samples.

Entry	P3HT						PNDIT2					
	$T_m/$ °C	$\Delta H_m/$ J/g <sup>b</sup>	$T_c/$ °C	$\Delta H_c/$ J/g <sup>b</sup>	$\Phi_{c,rel}/$ % <sup>c</sup>	$\Phi_{c,abs}/$ % <sup>d</sup>	$T_m/$ °C	$\Delta H_m/$ J/g <sup>b</sup>	$T_c/$ °C	$\Delta H_c/$ J/g <sup>b</sup>	$\Phi_{c,rel}/$ % <sup>c</sup>	
<b>3a</b>	227	21.6	197	21.6	100	65	--	--	--	--	--	
PNDIT2	--	--	--	--	--	--	308	8.7	289	9.3	100	
blend <sup>a</sup>	228	24.4	185	23.0	106	70	298	7.4	281	7.8	84	
<b>4a-23K</b>	224	9.1	162	8.2	38	25	297	3.4	268	3.4	37	
<b>4a-49K</b>	222	10.0	166	8.4	39	25	289	3.7	262	4.5	48	
<b>4a-57K</b>	229	9.6	164	7.9	37	24	292	5.9	264	7.2	77	
<b>4c-19K</b>	212	16.7	160	10.9	50	33	284	2.7	265	3.1	33	
<b>4c-42K</b>	222	13.2	169	11.2	52	34	288	4.7	259	6.7	72	
<b>4c-57K</b>	204	5.7	155	5.1	24	15	281	3.8	232	7.2	77	

<sup>a</sup>Preparation from P3HT (comparable to **3a**,  $M_{n,SEC} = 11$  kg/mol,  $\bar{D} = 1.1$ , 40 wt %) and PNDIT2 (same as used homopolymer,  $M_{n,SEC} = 28$  kg/mol,  $\bar{D} = 2.8$ , 60 wt %). <sup>b</sup>Enthalpies normalized by weight fractions. <sup>c</sup>Relative degree of crystallization compared to homopolymers, <sup>d</sup>absolute degree of crystallization with 100% crystalline P3HT corresponding to  $\Delta H_c = 33 \pm 3$  J/g.<sup>52</sup>

Further detailed analysis of optical properties, OPV device performances and morphological behavior of block copolymers, with respect to the influence of the DPP junction functionalization, are performed exclusively with the two samples **4a-49K** and **4c-42K**, hence we abbreviate by omitting the molecular weight and just use **4a** and **4c** for more clarity, respectively.

Optical properties of the BCP solutions and thin films were investigated by steady state UV-vis spectroscopy (Figure 5).

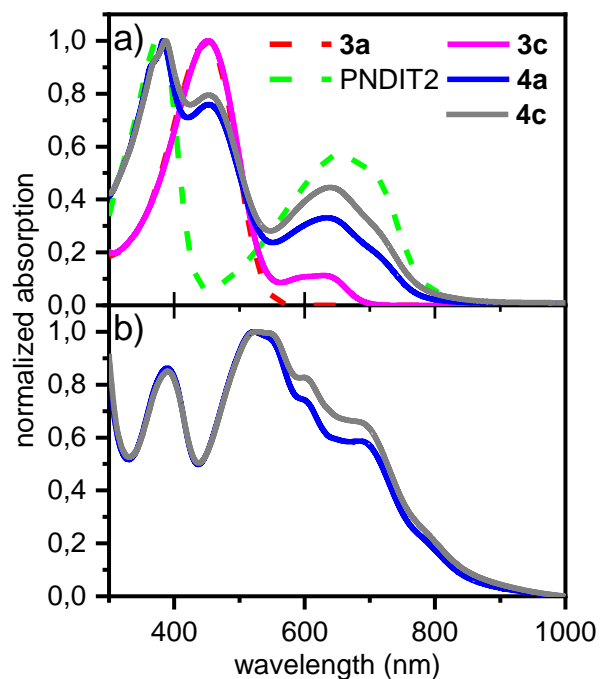


**Figure 5.** Normalized UV-vis spectra of a) P3HT-Th (**3a**), PNDIT2, H-P3HT-Th<sub>2</sub>DPPTTh<sub>2</sub> (**3c**) and BCPs **4a** and **4c** in solution (CHCl<sub>3</sub>, 0.02 mg/mL) and b) thin films of **4a** and **4c** annealed at 310 °C for 20 minutes under nitrogen (dashed).

Solution UV-vis spectrum shows a new charge transfer (CT) absorption band for **3c** between 580 and 700 nm due to the DPP end group. BCP samples with (**4c**) and without DPP (**4a**) combine all features of both homopolymers and show therefore a broad absorption over the entire visible range of the spectra. Besides the two  $\pi$ - $\pi^*$  transitions of P3HT and PNDIT2 at 387 and 453 nm, respectively, a broad CT absorption band at 620 nm of PNDIT2 can be observed. In the case of **4c**, the CT band of PNDIT2 overlaps with the absorption of the DPP moiety, resulting in a qualitatively similar absorption behavior of both BCPs **4a** and **4c**, but with increased absorption intensity between 500-700 nm in the latter system.

Thin films show broader and stronger absorption up to 900 nm due to  $\pi$ - $\pi$  stacking and stronger aggregation, compared to solutions of BCPs. Melt-annealing of BCP thin films results in slightly enhanced shapes as can be seen in Figure SI-14 a).

Cyclic voltammetry measurements are depicted in Figure SI-15.

The materials were further analyzed by photoluminescence (PL) spectroscopy in solutions (Figure SI-14 b) and thin films (Figure 6).

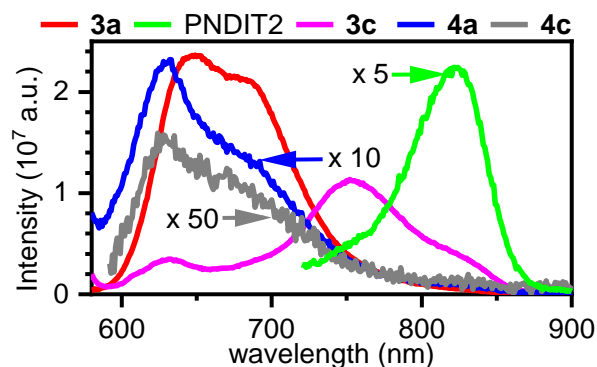


**Figure 6.** Thin film (annealed at 310 °C) PL spectra of P3HT-Th (**3a**), P3HT-Th<sub>2</sub>DPPTTh<sub>2</sub> (**3c**) and BCPs **4a** and **4c** in comparison with PNDIT2.

P3HT shows the well-known emission spectrum that decreases in intensity when melt-annealing is applied. The attachment of the Th<sub>2</sub>DPPTTh<sub>2</sub> end group in **3c** gives rise to a new emission band centered at 755 nm, and simultaneously quenches emission from P3HT, indicating electron or energy transfer into the covalently bound DPP end group. The strong electron accepting DPP group at the chain end forms a CT state to which the excitation is funneled, likely similar to benzothiadiazole-terminated P3HT.<sup>31</sup> Emission of both BCPs **4a** and **4c** is yet stronger quenched compared to both P3HT (**1**) and P3HT-Th<sub>2</sub>DPPTTh<sub>2</sub> (**3c**). Also, the CT emission band of **3c** is no longer seen in **4c**. This indicates an efficient electronic interaction between the block junction and the PNDIT2 block, caused by a covalent linkage with full retention of the

conjugation.<sup>34</sup> The residual BCP emission likely arises from the amorphous P3HT fraction that is not able to crystallize after melt-annealing. Considering the reduced melting and crystallization enthalpies of P3HT in all BCPs, the observation of amorphous P3HT emission must arise from regions which cannot transfer the excitation to either the interface or to crystalline P3HT, which has a smaller optical band gap.<sup>53</sup>

OPV devices were manufactured from P3HT:PNDIT2 blend (40:60 wt %) and BCP samples **4a** and **4c**. From each sample, the temperature-dependent device performance was investigated (Figure 7). The corresponding values are listed in Table SI-2-5, current-density voltage ( $JV$ ) curves are shown in Figure SI-16. In as-spun conditions, BCP **4c** shows the best power conversion efficiency ( $PCE$ ) of all three samples. Upon heating to 200 °C, all three samples behave differently. While the performance of the blend increases with increasing temperature up to  $T_m$  of P3HT, concomitant with  $PCE$ , the performance of **4c** remains almost constant and **4a** shows a clear drop in performance. Further annealing to above  $T_m$  of P3HT (250 °C) enhances  $J_{sc}$  and  $V_{oc}$  of the blend, but leads to a major drop in all parameters for both BCPs. Annealing at the highest temperature of 310 °C causes further decline of BCP device performance and also lowers performance of the blend.

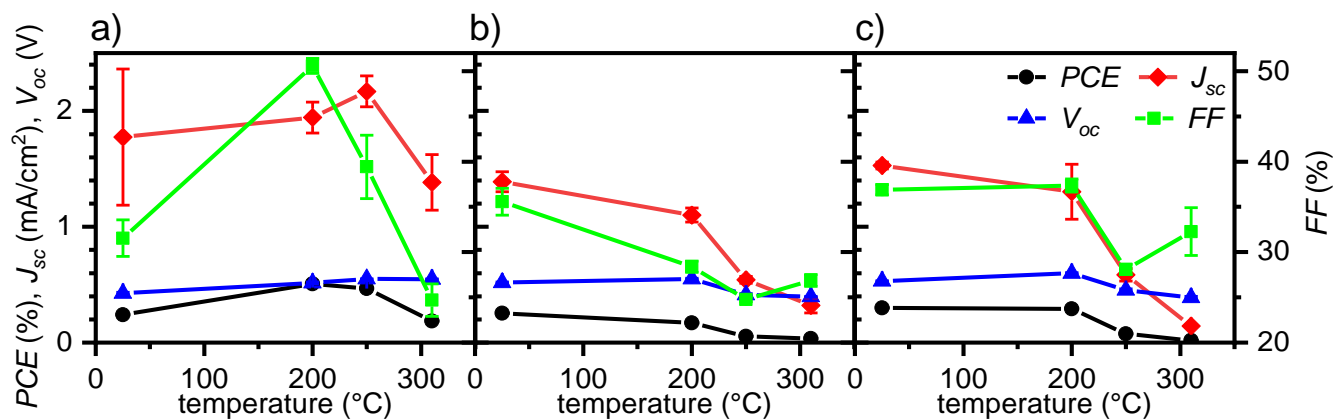


**Figure 7.** Temperature dependent OPV device performance of a) P3HT:PNDIT2 blend (40:60 wt %), b) **4a** and c) **4c**.

To gain further information about the morphological behavior of our BCP samples, we investigated thin films of **4c** by high-resolution transmission electron microscopy (HR-TEM). TEM bright field did not reveal a characteristic phase separated morphology arising from microphase separation in BCPs, but electron diffraction (ED) showed characteristic diffraction peaks of the P3HT blocks and the PNDIT2 block. The ED patterns of the as-spun films (Figure SI-17) show in general one single Scherrer ring at 24.8 Å that is indexed as (100)<sub>PNDIT2</sub>, indicating very poor organization of the copolymers. It is necessary to anneal the samples at a temperature of 250 °C to see a substantial change in the diffraction pattern with the appearance of additional Scherrer rings, as depicted in Figure 8. As seen in Table 3, the reflections can be indexed based on the known structures of PNDIT2 (form II) and P3HT (form I). However, the (100)<sub>P3HT</sub> peak in the copolymer films is observed at a distance of 17.5 Å that is substantially larger than the expected value of the (100)<sub>P3HT</sub> in a corresponding homopolymer (15.6 Å). The thermal annealing also results in a slight expansion of the d(100)<sub>PNDIT2</sub> from 24.8 Å in as-spun films to 25.9 Å after annealing at 250 °C. The co-existence of the (100) of P3HT and PNDIT2 indicates face-on orientation of both P3HT and PNDIT2 blocks. Both as-spun and 250 °C-annealed films show also the 7.1 Å reflection corresponding to the (002)<sub>PNDIT2</sub> that is dominant in form II with mixed stacks of NDI and T2.<sup>54</sup> A Scherrer ring at the  $\pi$ -stacking distance of 3.8 Å could also be observed indicating that some edge-on oriented P3HT is possibly present in the films annealed at 250 °C. Upon thermal annealing at 310 °C, the diffraction pattern changes substantially. It shows a very weak (002)<sub>PNDIT2</sub> and a large and dominant  $\pi$ -stacking reflection around 3.8 Å. Therefore, upon annealing to 310 °C, melt-recrystallization suppresses the initial dominant face-on orientation of the PNDIT2 block and causes a total reorientation of the crystals to edge-on for both P3HT and PNDIT2 blocks. This change in backbone orientation with

increasing temperature explains the drop in device performance for an increasing thermal annealing temperature. Thus, thermal annealing is usually necessary to induce segmental mobility and promote microphase separation in double crystalline BCPs and simultaneously leads to backbone reorientation, here for both blocks P3HT and PNDIT2. It is interesting to note that not all BCPs behave in this way. For example, P3HT-*block*-PCDTBT with the PCDTBT carrying semifluorinated side chains retains a face-on orientation also after melt-annealing.<sup>25</sup> However, the overall intensities of the reflections in copolymer films are weak and suggest a constrained crystallization of both blocks in the copolymer as compared to the blend of the two corresponding homopolymers. Obviously the diverse reorganization processes in all-conjugated, all-crystalline BCPs are mutually dependent and probably require highly sophisticated processing techniques and even more careful choice of building blocks.

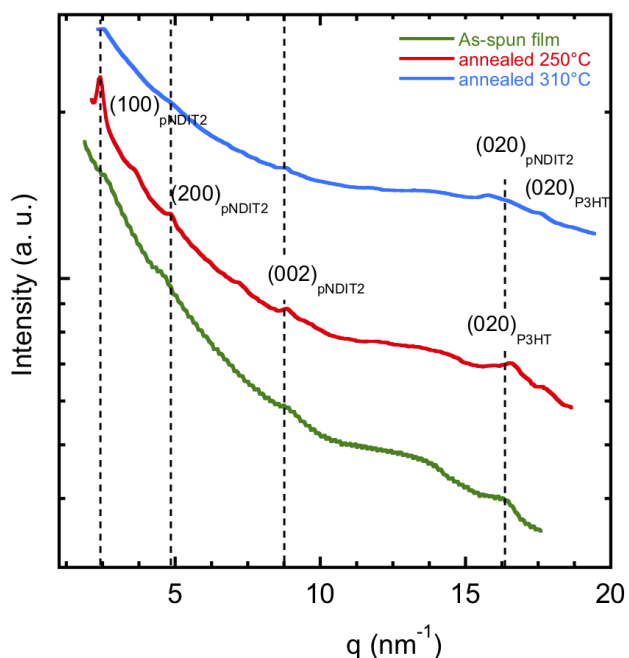


**Figure 8:** Temperature dependent angularly-averaged section profiles of sample **4c** from electron diffraction are presented with the indexation of the most important reflections (see Table 3).

**Table 3.** TEM reflections of both polymer blocks in **4c** in dependence of temperature treatment.

Condition	(100) <sub>PNDIT2</sub> / Å	(100) <sub>P3HT</sub> / Å	(200) <sub>PNDIT2</sub> / Å	(002) <sub>PNDIT2</sub> / Å	(020) <sub>PNDIT2</sub> / Å	(020) <sub>P3HT</sub> / Å
as-spun	24.8	--	--	7.1	--	3.8
250 °C	25.9	17.5	13.1	7.1	--	3,8/3.5
310 °C	--	--	--	7.1	--	3.8/3.5

Further information about microphase separation was sought by employing resonant soft X-ray scattering (RSoXS). By utilizing X-ray energies that match the core electron transitions of constituent atoms that occur in one block exclusively, RSoXS is able to provide elemental selectivity and chemical sensitivity to exploit differences in absorption between different phases, thus providing scattering signals with enhanced contrast.<sup>55</sup> Here, we report the application of RSoXS to characterize annealed thin films of **4a** and **4c**, processed under the same conditions used for OPV devices and TEM (310 °C).

Figure 9 presents the RSoXS data plotted as  $I(q)q^2$  for 284 eV (near the carbon absorption edge, where scattering contrast is enhanced). **4c** shows a slightly stronger peak compared to that of **4a**, suggesting that DPP junction functionalization results in a more defined structure at this molecular weight. Nevertheless, the peak location for both **4c** and **4a** appear at around  $q = 0.10 \text{ nm}^{-1}$ , corresponding to a 60 nm domain spacing, or about 30 nm domain size if equal thicknesses of P3HT and PNDIT2 domains are assumed. RSoXS data for all BCP samples with different molecular weights are summarized in Figure SI-18.

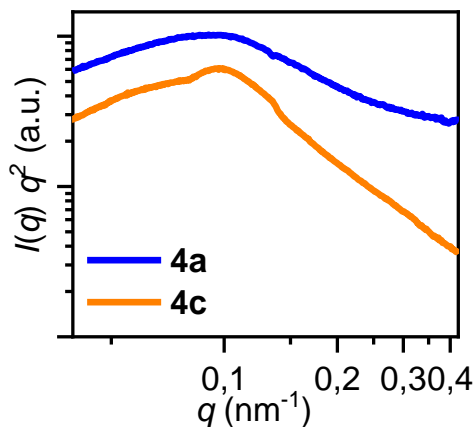


**Figure 9.**  $I(q)q^2$  vs  $q$  RSoXS curves for **4a** and **4c**.

For DPP junction functionalized BCP series **4c**, domain spacing increases from 42 to 70 nm with molar mass while for **4a** the three molar masses exhibit values between 57- 60 nm. The origin of this weak dependence of domain spacing on molar mass of series **4a** is currently unclear. The broad and relatively weak scattering signal is an indication for either weak microphase separation, kinetically trapped disorder, or disruption of mesoscale order due to crystallization of both blocks. An estimation of the contour length of P3HT gives 28 nm for the chain length used here.<sup>56</sup> The addition of a PNDIT2 segment with DP~ 10 would result in an overall contour length of 28 + 14 nm = 42 nm. Assuming chain extended crystals and considering the increase of molar mass within series **4c**, the experimental domain spacings between 47- 70 nm agree reasonably well with the size of BCP chains. Thus, RSoXS data provides a signal at the 60 nm scale not visible from TEM, which we interpret as microphase separation and semicrystalline (nearly chain extended) domains. At the same time, DSC indicates a reduced degree of crystallinity for both P3HT and PNDIT2, which makes this comparison less straightforward.

Femtosecond transient absorption (TA) spectroscopy was employed to characterize the influence of the modified BCP junction as well as the major performance limiting steps following photoexcitation of the as-spun blend and copolymer films. The pump fluence ( $2.5 \mu\text{J cm}^{-2}$ ) was selected to minimize the contribution of exciton-exciton annihilation to the observed kinetics (Figure SI-19). TA maps, containing the raw spectral and temporal information, are provided in Figure SI-20. Photoexcitation of the pure P3HT donor (at 560 nm) and PNDIT2 acceptor (at 700 nm) films generates broad photo-induced absorption features in the near infrared ( $\sim 850\text{-}1350 \text{ nm}$ ) which are characteristic of excitons in conjugated polymers.<sup>57</sup> These initial excitonic states fully decay within 100 ps. Upon blending or copolymerization of the donor and acceptor blocks, long-lived polaronic features, situated in the  $\sim 875\text{-}1100 \text{ nm}$  region, are shown to emerge.

In order to separate the spectrally-overlapping excitonic and polaronic responses, and identify additional intermediate states, we applied a global analysis (GA) procedure to the data sets (see Supporting Informations). For the P3HT:PNDIT2 blend, H-P3HT-Th-*block*-PNDIT2 (**4a**) and H-P3HT-Th<sub>2</sub>DPPTTh<sub>2</sub>-*block*-PNDIT2 (**4c**), the TA data can be deconvoluted into three distinct populations, each possessing unique spectral responses with overall shapes and peak positions that are common across all three material systems (Figure SI-21). These individual populations possess different decay profiles (short, intermediate and long-lived), a pattern that is also maintained across the three data sets. The evolution of the spectral responses, portrayed by these timescales, can be intuitively applied to the conventional model for OPV operation, depicted in Figure 10 as follows; (i) photogeneration of an initial short-lived exciton, (ii) charge transfer at the donor-acceptor interface to form an intermediate charge-transfer state (CTS) and (iii) dissociation of the CTS into long-lived free carriers (FCs).<sup>58</sup> Ultrafast ( $<1 \text{ ps}$ ) energy transfer can

also be incorporated into this mechanism when considering donor excitation (observed when selectively pumping P3HT in Figure SI-20).

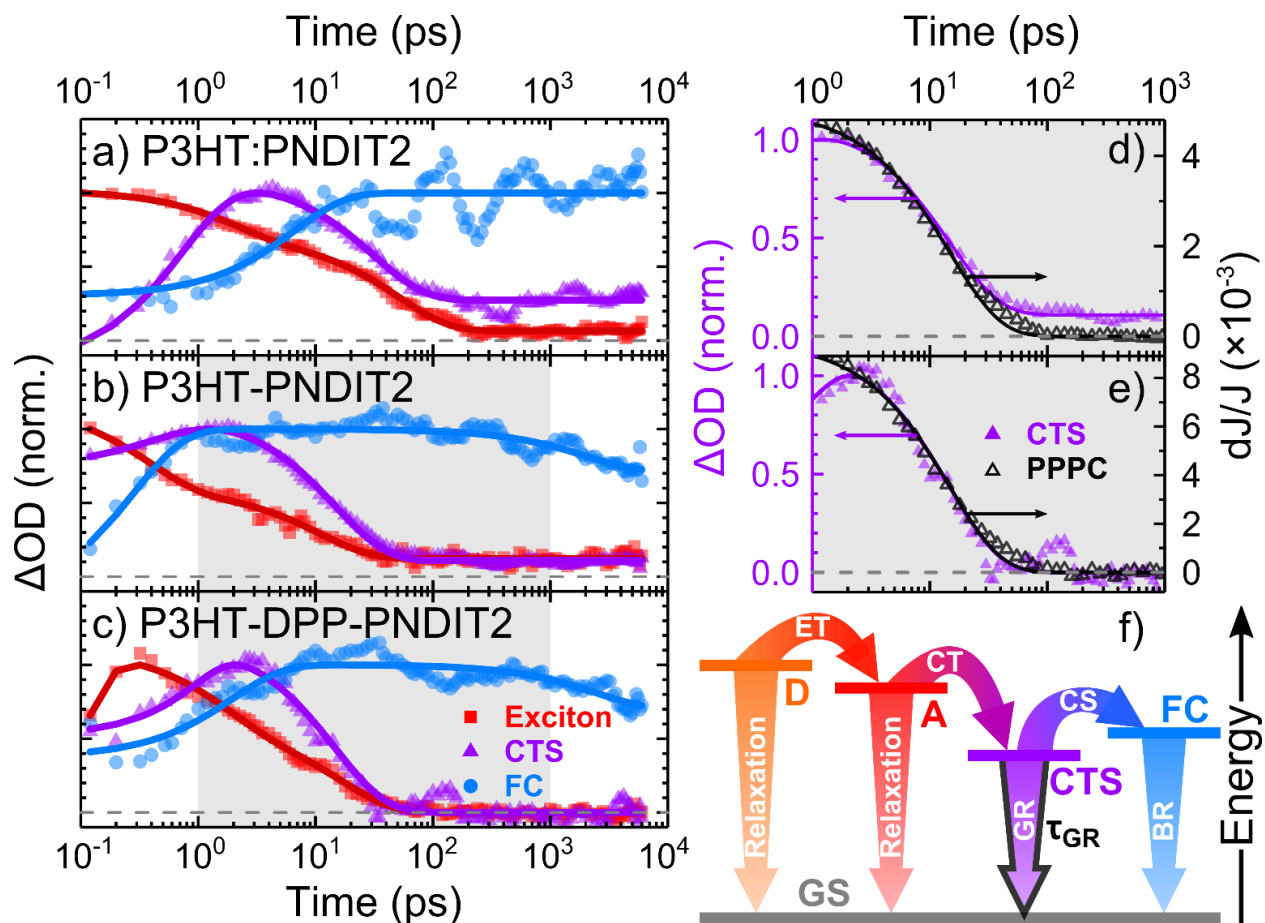


**Figure 10.** Transient absorption kinetics of exciton, charge transfer state (CTS) and free carriers (FC) in the blend (a), copolymer (b) and junction-functionalized copolymer (c), derived from global analysis. Pump-push-photocurrent (PPPC) transients from the P3HT-Th-*block*-PNDIT2 (4a) (d) and P3HT-Th<sub>2</sub>DPPTTh<sub>2</sub>-*block*-PNDIT2 (4c) (e) devices. A state diagram, describing the underlying photophysics (f) shows energy transfer (ET) from donor (D) to acceptor (A); charge (hole) transfer (CT); charge separation (CS) to form FCs; GR and bimolecular recombination (BR) to the ground state (GS). GR is highlighted as the dominant loss pathway, with a characteristic lifetime  $\tau_{GR}$ .

From the presented GA results (Figure 10 a-c), it is evident that the decay of the intermediate CTS does not correlate with the rise of the subsequent FCs, particularly in the copolymer systems. This indicates the interplay of an additional, detrimental pathway influencing the branching between CTS and FC, namely, the GR of bound CTSs. Figure 10 d-e) shows pump-push-photocurrent (PPPC) transients for the block copolymer-based devices. The dynamics are identical to the CTS dynamics extracted from GA. Furthermore, the magnitude of the transients ( $dJ/J$ ) is very high (on the order of  $10^{-3}$ ), illustrating the drastic enhancement of charge separation by the imposed dissociation of bound CTSs. Both these observations are hallmarks of pronounced GR in the studied devices.<sup>59</sup>

Since GR is the dominant loss pathway, it is worth remarking on the GR lifetimes ( $\tau_{GR}$ ) in each of the samples. For the blend,  $\tau_{GR}$  is  $\sim 30$  ps, and for both copolymers regardless of the DPP junction,  $\tau_{GR}$  is  $\sim 15$  ps. Differences in GR rates usually invoke the effects of morphology<sup>60</sup> or electron-hole coupling.<sup>61</sup> Enhanced phase segregation in the block copolymer materials (Figure 8) ought to extend the CT lifetime, which would undermine the former explanation. To this end, the weakly phase separated morphology and also the reduced degree of crystallinity present for P3HT and PNDIT2 segments in both **4a** and **4c** may be at the origin of this finding. On the other hand, the covalent linkage of donor and acceptor blocks has been demonstrated to enhance charge recombination rates in organic materials.<sup>62</sup> We therefore speculate that the electronic coupling is chiefly responsible. The invisible effect of the DPP junction tells us that the factor limiting lifetime and causing GR is another, likely morphological one. In any case, the promotion of GR in the block copolymer-based devices can explain the overall decrease in  $J_{sc}$  and  $FF$  without a similar compromise to the  $V_{oc}$ <sup>63</sup> (Figure 7).

## CONCLUSION

We have presented the design, synthesis and detailed characterization of junction-functionalized all-conjugated, double crystalline donor-acceptor block copolymers (BCPs). P3HT, Th<sub>2</sub>DPPT<sub>2</sub> and PNDIT2 were selected as the donor, junction and acceptor, respectively to yield an energy cascading structure. Regarding synthesis, all C-C coupling steps except P3HT synthesis were successfully accomplished through C-H activation. Complete end group functionalization of H-P3HT-Br was achieved with thienylated Th<sub>x</sub>DPPT<sub>x</sub> (x=1, 2). Sufficient high C-H end group reactivity using P3HT-Th<sub>2</sub>DPPT<sub>2</sub>-H and thus efficient junction incorporation into BCPs of type P3HT-Th<sub>2</sub>DPPT<sub>2</sub>-*block*-PNDIT2 was achieved.

Steady state absorption of H-P3HT-Th<sub>2</sub>DPPT<sub>2</sub> thin film revealed an additional bathochromically shifted charge transfer (CT) band due to the electron-deficient DPP unit at the chain end. Emission occurs almost entirely from this CT state, with P3HT emission being largely quenched. Further quenching of the emission including this CT state, occurs in the BCPs, and the residual emission is ascribed to amorphous P3HT, pointing to reduced P3HT crystallinity in the BCPs. This finding is fully confirmed by calorimetry and advanced scattering experiments (HR-TEM, RSoXS) that consistently showed a lower degree of crystallinity of P3HT and PNDIT2 in the BCPs compared to homopolymers, and a weak microphase separation at the length scale of 60 nm. Crystallinity and microphase separation was not influenced by the presence of the block junction. Thermal annealing promoted crystallinity but simultaneously changed backbone orientation in both BCPs from face-on in as-spun films to edge-on in melt-annealed films.

The unfavorable BCP backbone reorientation from face-on to edge-on is also the reason why OPV device performance decreases with increasing annealing temperature. It may well be the case that the unfavorable morphology and backbone orientation makes any electronic effect of DPP block junction functionalization invisible. From time-resolved spectroscopy, fast charge

separation and fast recombination was determined for both BCPs, independent of the block junction. As a higher degree of crystallinity and the presence of bicontinuous percolation pathways are known as key factors for preventing recombination, the presence of reduced crystalline and less ordered P3HT and PNDIT2 domains may override beneficial effect of the block junction regarding the suppression of charge recombination.

A general strategy to improve such materials is therefore to control microphase separation, the degree of crystallinity as well as block junction chemistry. At the same time, a face-on backbone orientation is required. Equally important is the design of systems that do not change backbone orientation during melt-annealing. Control over these two factors is necessary to investigate electronic effects by time-resolved spectroscopy at well-defined BCP junctions of whichever chemical nature. To this end, elucidating the effect of conjugation between the three components on energy levels and electronic properties will reveal the presence and nature of a possible cascading landscape at the donor-acceptor interface.

## ASSOCIATED CONTENT

**Supporting Information.** Syntheses details of Th<sub>2</sub>DPPT<sub>2</sub> (**2c**), optimization of H-P3HT-ThDPPT<sub>2</sub> (**3b**) synthesis and characterization including H-P3HT-Th<sub>2</sub>DPPT<sub>2</sub> (**3c**) by SEC, MALDI-ToF MS, NMR, UV-vis and PL spectroscopy and further analyses of BCPs **4a** and **4c** by cyclic voltammetry, NMR spectroscopy, HR-TEM, RSoXS, TAS and OPV characteristics. This material is available free of charge via the Internet at <http://pubs.acs.org>.

## AUTHOR INFORMATION

### Corresponding Author

\*E-mail [Michael.sommer@chemie.tu-chemnitz.de](mailto:Michael.sommer@chemie.tu-chemnitz.de) (M.S.)

## **ORCID**

Thomas R. Hopper: 0000-0001-5084-1914

Simon B. Schmidt: 0000-0002-1119-0212

Artem A. Bakulin: 0000-0002-3998-2000

Hartmut Komber: 0000-0001-6176-6737

Michael Sommer: 0000-0002-2377-5998

## **Author Contributions**

The manuscript was written through contributions of all authors. All authors have given approval to the final version of the manuscript.

## **Funding Sources**

The Baden-Württemberg Stiftung gGmbH (research program Clean Tech 2, project CT 2) and the Research Innovation Fund of the University of Freiburg is gratefully acknowledged for funding. BK and EDG acknowledge the National Science Foundation for funding under Award DMR-1609417.

## **Notes**

The authors declare no competing financial interest.

## **ACKNOWLEDGMENT**

The authors are grateful to M. Hagios, Dr. R. Hanselmann, C. Warth and A. Warmbold (University of Freiburg) for SEC, MALDI-ToF MS and DSC measurements, respectively. Further, Dr. P. Shakya Tuladhar (Imperial College London) is greatly acknowledged for OPV device manufacturing. A.A.B. is a Royal Society University Research Fellow. The Advanced

Light Source is supported by the Director, Office of Science, Office of Basic Energy Science, of the U.S. Department of Energy under Contract No. DE-AC02-05CH11231.

## REFERENCES

- (1) Holliday, S.; Li, Y.; Luscombe, C. K. Recent Advances in High Performance Donor-Acceptor Polymers for Organic Photovoltaics. *Prog. Polym. Sci.* **2017**, *70*, 34–51.
- (2) Lee, C.; Li, Y.; Lee, W.; Lee, Y.; Choi, J.; Kim, T.; Wang, C.; Gomez, E. D.; Woo, H. Y.; Kim, B. J. Correlation between Phase-Separated Domain Sizes of Active Layer and Photovoltaic Performances in All-Polymer Solar Cells. *Macromolecules* **2016**, *49* (14), 5051–5058.
- (3) McNeill, C. R.; Westenhoff, S.; Groves, C.; Friend, R. H.; Greenham, N. C. Influence of Nanoscale Phase Separation on the Charge Generation Dynamics and Photovoltaic Performance of Conjugated Polymer Blends: Balancing Charge Generation and Separation. *J. Phys. Chem. C* **2007**, *111* (51), 19153–19160.
- (4) McNeill, C. R. Morphology of All-Polymer Solar Cells. *Energy Environ. Sci.* **2012**, *5* (2), 5653.
- (5) Zhou, N.; Lin, H.; Lou, S. J.; Yu, X.; Guo, P.; Manley, E. F.; Loser, S.; Hartnett, P.; Huang, H.; Wasielewski, M. R.; et al. Morphology-Performance Relationships in High-Efficiency All-Polymer Solar Cells. *Adv. Energy Mater.* **2014**, *4* (3), 1300785.
- (6) Benten, H.; Mori, D.; Ohkita, H.; Ito, S. Recent Research Progress of Polymer Donor/Polymer Acceptor Blend Solar Cells. *J. Mater. Chem. A* **2016**, *4* (15), 5340–5365.
- (7) Lu, L.; Kelly, M. A.; You, W.; Yu, L. Status and Prospects for Ternary Organic Photovoltaics. *Nat. Photonics* **2015**, *9* (8), 491–500.
- (8) Xing, S.; Wang, H.; Zheng, Y.; Yu, J. Förster Resonance Energy Transfer and Energy

- Cascade with a Favorable Small Molecule in Ternary Polymer Solar Cells. *Sol. Energy* **2016**, *139*, 221–227.
- (9) Heidel, T. D.; Hochbaum, D.; Sussman, J. M.; Singh, V.; Bahlke, M. E.; Hiromi, I.; Lee, J.; Baldo, M. A. Reducing Recombination Losses in Planar Organic Photovoltaic Cells Using Multiple Step Charge Separation. *J. Appl. Phys.* **2011**, *109* (10), 104502.
- (10) Schlenker, C. W.; Barlier, V. S.; Chin, S. W.; Whited, M. T.; McAnally, R. E.; Forrest, S. R.; Thompson, M. E. Cascade Organic Solar Cells. *Chem. Mater.* **2011**, *23* (18), 4132–4140.
- (11) Endres, J.; Pelczar, I.; Rand, B. P.; Kahn, A. Determination of Energy Level Alignment within an Energy Cascade Organic Solar Cell. *Chem. Mater.* **2016**, *28* (3), 794–801.
- (12) Tan, Z. K.; Johnson, K.; Vaynzof, Y.; Bakulin, A. a.; Chua, L. L.; Ho, P. K. H.; Friend, R. H. Suppressing Recombination in Polymer Photovoltaic Devices via Energy-Level Cascades. *Adv. Mater.* **2013**, *25* (30), 4131–4138.
- (13) Bates, C. M.; Bates, F. S. 50th Anniversary Perspective : Block Polymers—Pure Potential. *Macromolecules* **2017**, *50* (1), 3–22.
- (14) Ruzette, A.-V.; Leibler, L. Block Copolymers in Tomorrow's Plastics. *Nat. Mater.* **2005**, *4* (1), 19–31.
- (15) Schlotthauer, T.; Schroot, R.; Glover, S.; Hammarström, L.; Jäger, M.; Schubert, U. S. A Multidonor–photosensitizer–multiacceptor Triad for Long-Lived Directional Charge Separation. *Phys. Chem. Chem. Phys.* **2017**, *19* (42), 28572–28578.
- (16) Schroot, R.; Schlotthauer, T.; Dietzek, B.; Jäger, M.; Schubert, U. S. Extending Long-Lived Charge Separation Between Donor and Acceptor Blocks in Novel Copolymer Architectures Featuring a Sensitizer Core. *Chem. - A Eur. J.* **2017**, *23* (65), 16484–16490.

- (17) Scherf, U.; Gutacker, A.; Koenen, N. All-Conjugated Block Copolymers. *Acc. Chem. Res.* **2008**, *41* (9), 1086–1097.
- (18) Sommer, M.; Huettner, S.; Thelakkat, M. Donor–acceptor Block Copolymers for Photovoltaic Applications. *J. Mater. Chem.* **2010**, *20* (48), 10788.
- (19) Segalman, R. A.; McCulloch, B.; Kirmayer, S.; Urban, J. J. Block Copolymers for Organic Optoelectronics. *Macromolecules* **2009**, *42* (23), 9205–9216.
- (20) Lee, Y.; Gomez, E. D. Challenges and Opportunities in the Development of Conjugated Block Copolymers for Photovoltaics. *Macromolecules* **2015**, *48* (20), 7385–7395.
- (21) Lohwasser, R. H.; Gupta, G.; Kohn, P.; Sommer, M.; Lang, A. S.; Thurn-Albrecht, T.; Thelakkat, M. Phase Separation in the Melt and Confined Crystallization as the Key to Well-Ordered Microphase Separated Donor–Acceptor Block Copolymers. *Macromolecules* **2013**, *46* (11), 4403–4410.
- (22) Tkachov, R.; Komber, H.; Rauch, S.; Lederer, A.; Oertel, U.; Häußler, L.; Voit, B.; Kiriy, A. One-Pot Synthesis of All-Conjugated Block-Like Bisthiophene–Naphthalenediimide/Fluorene Copolymer. *Macromolecules* **2014**, *47* (15), 4994–5001.
- (23) Bridges, C. R.; Yan, H.; Pollit, A. A.; Seferos, D. S. Controlled Synthesis of Fully  $\pi$ -Conjugated Donor–Acceptor Block Copolymers Using a Ni(II) Diimine Catalyst. *ACS Macro Lett.* **2014**, *3* (7), 671–674.
- (24) Sommer, M.; Komber, H.; Huettner, S.; Mulherin, R.; Kohn, P.; Greenham, N. C.; Huck, W. T. S. Synthesis, Purification, and Characterization of Well-Defined All-Conjugated Diblock Copolymers PF8TBT- b -P3HT. *Macromolecules* **2012**, *45* (10), 4142–4151.
- (25) Lombeck, F.; Komber, H.; Sepe, A.; Friend, R. H.; Sommer, M. Enhancing Phase Separation and Photovoltaic Performance of All-Conjugated Donor–Acceptor Block

- Copolymers with Semifluorinated Alkyl Side Chains. *Macromolecules* **2015**, *48* (21), 7851–7860.
- (26) Tu, G.; Li, H.; Forster, M.; Heiderhoff, R.; Balk, L. J.; Scherf, U. Conjugated Triblock Copolymers Containing Both Electron-Donor and Electron-Acceptor Blocks. *Macromolecules* **2006**, *39* (13), 4327–4331.
- (27) Verduzco, R.; Botiz, I.; Pickel, D. L.; Kilbey, S. M.; Hong, K.; Dimasi, E.; Darling, S. B. Polythiophene- Block -Polyfluorene and Polythiophene- Block -Poly(Fluorene- Co - Benzothiadiazole): Insights into the Self-Assembly of All-Conjugated Block Copolymers. *Macromolecules* **2011**, *44* (3), 530–539.
- (28) Lee, Y.; Aplan, M. P.; Seibers, Z. D.; Kilbey, S. M.; Wang, Q.; Gomez, E. D. Tuning the Synthesis of Fully Conjugated Block Copolymers to Minimize Architectural Heterogeneity. *J. Mater. Chem. A* **2017**, *5* (38), 20412–20421.
- (29) Ku, S.-Y.; Brady, M. a.; Treat, N. D.; Cochran, J. E.; Robb, M. J.; Kramer, E. J.; Chabynyc, M. L.; Hawker, C. J. A Modular Strategy for Fully Conjugated Donor–Acceptor Block Copolymers. *J. Am. Chem. Soc.* **2012**, *134* (38), 16040–16046.
- (30) Mulherin, R. C.; Jung, S.; Huettner, S.; Johnson, K.; Kohn, P.; Sommer, M.; Allard, S.; Scherf, U.; Greenham, N. C. Ternary Photovoltaic Blends Incorporating an All-Conjugated Donor–Acceptor Diblock Copolymer. *Nano Lett.* **2011**, *11* (11), 4846–4851.
- (31) Johnson, K.; Huang, Y.-S.; Huettner, S.; Sommer, M.; Brinkmann, M.; Mulherin, R.; Niedzialek, D.; Beljonne, D.; Clark, J.; Huck, W. T. S.; et al. Control of Intrachain Charge Transfer in Model Systems for Block Copolymer Photovoltaic Materials. *J. Am. Chem. Soc.* **2013**, *135* (13), 5074–5083.
- (32) Mok, J. W.; Lin, Y.-H.; Yager, K. G.; Mohite, A. D.; Nie, W.; Darling, S. B.; Lee, Y.;

- Gomez, E.; Gosztola, D.; Schaller, R. D.; et al. Linking Group Influences Charge Separation and Recombination in All-Conjugated Block Copolymer Photovoltaics. *Adv. Funct. Mater.* **2015**, *25* (35), 5578–5585.
- (33) Wang, Y.; Wang, Q.; Zhan, X.; Wang, F.; Safdar, M.; He, J. Visible Light Driven Type II Heterostructures and Their Enhanced Photocatalysis Properties: A Review. *Nanoscale* **2013**, *5* (18), 8326.
- (34) Nübling, F.; Komber, H.; Sommer, M. All-Conjugated, All-Crystalline Donor–Acceptor Block Copolymers P3HT-*b*-PNDIT2 via Direct Arylation Polycondensation. *Macromolecules* **2017**, *50* (5), 1909–1918.
- (35) Chua, L.-L.; Zaumseil, J.; Chang, J.-F.; Ou, E. C.-W.; Ho, P. K.-H.; Sirringhaus, H.; Friend, R. H. General Observation of N-Type Field-Effect Behaviour in Organic Semiconductors. *Nature* **2005**, *434* (7030), 194–199.
- (36) Fabiano, S.; Chen, Z.; Vahedi, S.; Facchetti, A.; Pignataro, B.; Loi, M. a. Role of Photoactive Layer Morphology in High Fill Factor All-Polymer Bulk Heterojunction Solar Cells. *J. Mater. Chem.* **2011**, *21* (16), 5891.
- (37) Matsidik, R.; Luzio, A.; Askin, Ö.; Fazzi, D.; Sepe, A.; Steiner, U.; Komber, H.; Caironi, M.; Sommer, M. Highly Planarized Naphthalene Diimide–Bifuran Copolymers with Unexpected Charge Transport Performance. *Chem. Mater.* **2017**, *29* (13), 5473–5483.
- (38) Tamayo, A. B.; Tantiwivat, M.; Walker, B.; Nguyen, T. Design, Synthesis, and Self-Assembly of Oligothiophene Derivatives with a Diketopyrrolopyrrole Core. *J. Phys. Chem. C* **2008**, *112* (39), 15543–15552.
- (39) Bürckstümmer, H.; Weissenstein, A.; Bialas, D.; Würthner, F. Synthesis and Characterization of Optical and Redox Properties of Bithiophene-Functionalized

- Diketopyrrolopyrrole Chromophores. *J. Org. Chem.* **2011**, *76* (8), 2426–2432.
- (40) Zalesskiy, S. S.; Ananikov, V. P. Pd<sub>2</sub>(Dba)<sub>3</sub> as a Precursor of Soluble Metal Complexes and Nanoparticles: Determination of Palladium Active Species for Catalysis and Synthesis. *Organometallics* **2012**, *31* (6), 2302–2309.
- (41) Hendsbee, A. D.; Sun, J.-P.; Rutledge, L. R.; Hill, I. G.; Welch, G. C. Electron Deficient Diketopyrrolopyrrole Dyes for Organic Electronics: Synthesis by Direct Arylation, Optoelectronic Characterization, and Charge Carrier Mobility. *J. Mater. Chem. A* **2014**, *2* (12), 4198.
- (42) Sahu, D.; Tsai, C.-H.; Wei, H.-Y.; Ho, K.-C.; Chang, F.-C.; Chu, C.-W. Synthesis and Applications of Novel Low Bandgap Star-Burst Molecules Containing a Triphenylamine Core and Dialkylated Diketopyrrolopyrrole Arms for Organic Photovoltaics. *J. Mater. Chem.* **2012**, *22* (16), 7945.
- (43) Gao, H.; Li, Y.; Wang, L.; Ji, C.; Wang, Y.; Tian, W.; Yang, X.; Yin, L. High Performance Asymmetrical Push–pull Small Molecules End-Capped with Cyanophenyl for Solution-Processed Solar Cells. *Chem. Commun.* **2014**, *50* (71), 10251–10254.
- (44) Dou, L.; Gao, J.; Richard, E.; You, J.; Chen, C.-C.; Cha, K. C.; He, Y.; Li, G.; Yang, Y. Systematic Investigation of Benzodithiophene- and Diketopyrrolopyrrole-Based Low-Bandgap Polymers Designed for Single Junction and Tandem Polymer Solar Cells. *J. Am. Chem. Soc.* **2012**, *134* (24), 10071–10079.
- (45) Dienes, Y.; Durben, S.; Kárpáti, T.; Neumann, T.; Englert, U.; Nyulászi, L.; Baumgartner, T. Selective Tuning of the Band Gap of  $\pi$ -Conjugated Dithieno[3,2-6: 2',3'-d]Phospholes toward Different Emission Colors. *Chem. - A Eur. J.* **2007**, *13* (26), 7487–7500.
- (46) Lohwasser, R. H.; Thelakkat, M. Toward Perfect Control of End Groups and

- Polydispersity in Poly(3-Hexylthiophene) via Catalyst Transfer Polymerization. *Macromolecules* **2011**, *44* (9), 3388–3397.
- (47) Sasikumar, M.; Suseela, Y. V.; Govindaraju, T. Dibromohydantoin: A Convenient Brominating Reagent for 1,4,5,8-Naphthalenetetracarboxylic Dianhydride. *Asian J. Org. Chem.* **2013**, *2* (9), 779–785.
- (48) Kudla, C. J.; Dolfen, D.; Schottler, K. J.; Koenen, J.-M.; Breusov, D.; Allard, S.; Scherf, U. Cyclopentadithiazole-Based Monomers and Alternating Copolymers. *Macromolecules* **2010**, *43* (18), 7864–7867.
- (49) Brinkmann, M.; Rannou, P. Molecular Weight Dependence of Chain Packing and Semicrystalline Structure in Oriented Films of Regioregular Poly(3-Hexylthiophene) Revealed by High-Resolution Transmission Electron Microscopy. *Macromolecules* **2009**, *42* (4), 1125–1130.
- (50) Matsidik, R.; Komber, H.; Luzio, A.; Caironi, M.; Sommer, M. Defect-Free Naphthalene Diimide Bithiophene Copolymers with Controlled Molar Mass and High Performance via Direct Arylation Polycondensation. *J. Am. Chem. Soc.* **2015**, *137* (20), 6705–6711.
- (51) Panthani, T. R.; Bates, F. S. Crystallization and Mechanical Properties of Poly( $\epsilon$ -Lactide)-Based Rubbery/Semicrystalline Multiblock Copolymers. *Macromolecules* **2015**, *48* (13), 4529–4540.
- (52) Balko, J.; Lohwasser, R. H.; Sommer, M.; Thelakkat, M.; Thurn-Albrecht, T. Determination of the Crystallinity of Semicrystalline Poly(3-Hexylthiophene) by Means of Wide-Angle X-Ray Scattering. *Macromolecules* **2013**, *46* (24), 9642–9651.
- (53) Clark, J.; Silva, C.; Friend, R. H.; Spano, F. C. Role of Intermolecular Coupling in the Photophysics of Disordered Organic Semiconductors: Aggregate Emission in

- Regioregular Polythiophene. *Phys. Rev. Lett.* **2007**, *98* (20), 206406.
- (54) Brinkmann, M.; Gonthier, E.; Bogen, S.; Tremel, K.; Ludwigs, S.; Hufnagel, M.; Sommer, M. Segregated versus Mixed Interchain Stacking in Highly Oriented Films of Naphthalene Diimide Bithiophene Copolymers. *ACS Nano* **2012**, *6* (11), 10319–10326.
- (55) Wang, C.; Lee, D. H.; Hexemer, A.; Kim, M. I.; Zhao, W.; Hasegawa, H.; Ade, H.; Russell, T. P. Defining the Nanostructured Morphology of Triblock Copolymers Using Resonant Soft X-Ray Scattering. *Nano Lett.* **2011**, *11* (9), 3906–3911.
- (56) Brinkmann, M. Structure and Morphology Control in Thin Films of Regioregular Poly(3-Hexylthiophene). *J. Polym. Sci. Part B Polym. Phys.* **2011**, *49* (17), 1218–1233.
- (57) Guo, J.; Ohkita, H.; Benten, H.; Ito, S. Near-IR Femtosecond Transient Absorption Spectroscopy of Ultrafast Polaron and Triplet Exciton Formation in Polythiophene Films with Different Regioregularities. *J. Am. Chem. Soc.* **2009**, *131* (46), 16869–16880.
- (58) Clarke, T. M.; Durrant, J. R. Charge Photogeneration in Organic Solar Cells. *Chem. Rev.* **2010**, *110* (11), 6736–6767.
- (59) Zhang, J.; Gu, Q.; Do, T. T.; Rundel, K.; Sonar, P.; Friend, R. H.; McNeill, C. R.; Bakulin, A. A. Control of Geminate Recombination by the Material Composition and Processing Conditions in Novel Polymer: Nonfullerene Acceptor Photovoltaic Devices. *J. Phys. Chem. A* **2018**, *122* (5), 1253–1260.
- (60) Müller, J. G.; Lupton, J. M.; Feldmann, J.; Lemmer, U.; Scharber, M. C.; Sariciftci, N. S.; Brabec, C. J.; Scherf, U. Ultrafast Dynamics of Charge Carrier Photogeneration and Geminate Recombination in Conjugated Polymer:Fullerene Solar Cells. *Phys. Rev. B* **2005**, *72* (19), 195208.
- (61) Onsager, L. Initial Recombination of Ions. *Phys. Rev.* **1938**, *54* (8), 554–557.

- (62) Marcos Ramos, A.; Knol, J.; Meskers, S. C. J.; Hal, P. A. van; Hummelen, J. C.; Janssen, R. A. J. Photoinduced Multistep Energy and Electron Transfer in a Oligoaniline - Oligo (p-Phenylenevinylene) - Fullerene Triad. *J. Phys. Chem.* **2003**, *107*, 9269–9283.
- (63) Credgington, D.; Hamilton, R.; Atienzar, P.; Nelson, J.; Durrant, J. R. Non-Geminate Recombination as the Primary Determinant of Open-Circuit Voltage in Polythiophene:Fullerene Blend Solar Cells: An Analysis of the Influence of Device Processing Conditions. *Adv. Funct. Mater.* **2011**, *21* (14), 2744–2753.

## TABLE OF CONTENT

